NANO · MICRO small

Supporting Information

for *Small*, DOI 10.1002/smll.202303741

Writing Into Water

Nadir Möller, Lukas Hecht, Ran Niu, Benno Liebchen and Thomas Palberg**

WILEY-VCH

Supporting Information

Writing Into Water

Nadir Möller, Lukas Hecht, Ran Niu, Benno Liebchen, Thomas Palberg**

N. Möller, T. Palberg
Institut für Physik
Johannes Gutenberg Universität
Staudinger Weg 7
55128 Mainz, Germany
E-mail: palberg@uni-mainz.de

L. Hecht, B. Liebchen
Institute for Condensed Matter Physics
Department of Physics
Technische Universität Darmstadt
Hochschulstr. 8
64289 Darmstadt, Germany
E-mail: benno.liebchen@pkm.tu-darmstadt.de

R. Niu
Huazhong University of Science and Technology
Luoyu Road 1037
Wuhan, 430074, China

This PDF file includes:

Supporting Text
Figures S1 to S20
Captions of Movies S1 to S9

Other Supporting Information for this manuscript include the following:

Movies S1 to S9

Supporting Text

1. Additional Experimental Data

The modular character of our approach allows for a systematic test of line properties upon changing the experimental boundary conditions, the employed components, and the pen-drive. We first present our experiments performed for the C-IEX45/Si832 system, then turn to other combinations.

1.1. Variation of IEX speed

On an inclined substrate, ion-exchange resin bead (IEX) and tracers roll downward. Their speed is easily tuned by varying the substrate tilt angle ϑ. This is exemplarily shown in Figure S1a for C-IEX45 beads rolling in tracer-free water. Data are averaged over five beads. Error bars denote the statistical error in v_{IEX}, which increases with ϑ, and the systematic uncertainty in meeting the adjusted ϑ, which decreases with increasing ϑ.

Single lines are written in a speed range of 1.5 μm s^{-1} < v_{IEX} < 10 μm s^{-1}. At lower speeds, we observe the formation of an extended, asymmetric accretion zone immediately past the IEX (Figure 4c example IV, main text). Surplus tracers leave this region through a wide contour and no useful line is obtained. At larger speeds, the line occasionally shows an initial split into two parallel lines separated by only a small distance. These lines quickly merge by diffusion. For concentrations $c \geq 0.2$ wt.%, larger velocities are needed to generate the line split. We conclude that moderate speeds return the best results.

1.2. Line evolution past the line focus

The line width in the decay region depends on both the tracer concentration and the IEX speed. Figure S2a shows snapshots of C-IEX rolling through Si832. From top to bottom, the tracer concentration c increases, and the velocities vary in the range of v_{IEX} = 6-12 μm s^{-1}. With increasing c, the background intensity increases and the lines appear thicker.

For each line in Figure S2a, we recorded the intensity profiles 80 s after IEX passage, i.e., far past the line focus and show these in Figure S2b. For better statistics, we here averaged over a trail length of 50 μm. All five density profiles are well described by Gaussians superimposed on a flat background. The fits return the standard deviation σ, which relates to the Full Width at Half Maximum (FWHM) as 2.355σ = FWHM. From independent measurements on Si832 layers equilibrated at $\vartheta = 0$ and performed under exactly identical illumination, we found the dark field scattered intensity to increase with a power law dependence as $I \propto c^a$ (Figure S2c). Fitting a linear function to the data in the double logarithmic plot of Figure S2b returns an exponent of $a = 0.85 \pm 0.04$. This is close to but below the expectation of light scattering theory for dilute suspensions: $a = 1$. The observed small deviation is attributed to tracer-tracer repulsion, which leads to the development of fluid order and in turn, decreases the forward-scattering. Figure S2d shows the time-dependent FWHM extracted from the concentration-dependent experiments in Figure S2a. The black arrow marks t = 80 s used in Figure S2b. All curves increase roughly linearly in this double-logarithmic plot. The feature marked by the blue arrow is caused by the passage of a blob also seen in Figure S4a. As expected, the curves get wider for increasing concentrations, but the vertical spacing between the curves does not match exactly with the increase in weight fraction. This could be due to the different

velocities of the IEX in Figure S2a. We therefore determined the velocity dependence of line widths in independent measurements at constant tracer concentration.

Figure S2e shows the data for c = 0.18 wt.%. Here, we averaged over five to ten IEX beads per adjusted tilt angle. The large standard deviation in the measured IEX speed is attributed to the size dispersity of the IEX. The widths decrease systematically with increasing velocity. Data in this double logarithmic plot are well described by a power law with exponent -1.02 ± 0.09. This is remarkably close to -1. The comparably large uncertainty of the fit and the small deviation are again attributed to variations in IEX size. We use the result to rescale the data of Figure S2d to v_{IEX} = 8 µm s^{-1}. The velocity-scaled data sets are displayed in Figure S2f. The data sets are now spaced more evenly. The velocity-scaled FWHM at t = 80 s is shown in dependence on concentration in Figure S2g. The data in this double-logarithmic plot are well described by a power law of exponent a = 0.51 ± 0.02. We use the result to rescale the data in Figure S2f to c = 0.1 wt.%. The velocity- and concentration-scaled data are plotted double-logarithmically in Figure S2h versus time after IEX passage. All data arrange neatly along a single curve. Fitting a linear function to the data returns a power-law behavior FWHM $\propto t^{\lambda}$ with exponent λ = 0.48 ± 0.04. This is close to the theoretical expectation of λ = 0.5 for free diffusion.

We stress that these data were taken by averaging over only a few IEX at each inspected set of boundary conditions. The observed scaling behavior should therefore be taken with due caution. However, even these preliminary data are well compatible with a simple scaling behavior for the line width as FWHM $\propto v_{IEX}^{-1}\, c^{½}\, t^{½}$. The v-scaling would be expected as long as the IEX accretes the tracers with a constant solvent flux arriving at its surface. This is reasonable due to the large exchange capacity of the IEX and the low concentration of residual cations. The t-scaling is expected for a purely diffusive decay.

1.3. Shaping the formation zone

In this section, we consider the influences of tracer charge, substrate charge, and pH-gradient strength. For C-IEX45 rolling in Si832, we observe significant changes of the shape of the formation zone but no effects for the decay zone. The changes in the formation zone relate to a systematic variation in the approach-distance of the tracers.

The pH-gradient induces significant diffusio-osmotic (DO) flows along a highly charged substrate, which transport low-charge tracers towards the IEX. The approach velocity measured between 200 µm and 50 µm distance from the IEX center was used to describe this approach in terms of an effective attraction exerted by the IEX (Figure 3, main text). At shorter distances, the hydrodynamic flow pattern is significantly more complicated due to upward components in the solvent motion, the complex geometry of the wedge between IEX and substrate, hydrodynamic and direct tracer-tracer interactions, and the presence of an additional type of phoretic flow. In fact, low-charge or uncharged tracers are halted by these effects very close to or even underneath the IEX center. The exact stopping distance is not accessible in the flow field measurements due to shading by the IEX. We accounted for these phenomena in an effective way by adding a repulsive component to the total effective force.

The situation differs for highly charged tracers due to the additional diffusio-phoretic slip existing at their surface.[1,2] For this case, the approach situation is sketched in Figure S3. Relative to the tracer surface, the pH-gradient induces an additional inward solvent flow (DPS, dark blue arrow), which results in an outward tracer motion (DPT, violet arrow). In the sketched situation, the tracer would still be swept further inward towards the IEX. However,

with increasing gradient strength, v_{DPT} will increase until it equals v_{DO}, and the tracer becomes stalled.

To vary the relative weight of the two phoretic flows, we systematically varied the charge ratio $\chi = \zeta_T/\zeta_S$ between tracers and substrate. Experiments in the main text were performed with deionized tracer suspensions equilibrated in contact with ambient air. Due to CO_2 adsorption, their ζ-potential is low,[3] and diffusio-phoretic (DP) flows are of negligible magnitude except very close to the IEX surface, where the pH gradients are strongest. We de-carbonized the tracers and charged them up by prolonged batch deionization removing CO_2 through ion exchange of its dissociation products (carbonic acid). Further, a reduced substrate ζ-potential was obtained by storing the substrate slides in diluted deconex® cleaning solutions. A stepwise increase in charge ratio had a significant influence on the minimum approach distance. It drastically altered the shape of the formation zone but left the decay unaffected. This is shown in Figure S4a-d. For charge ratios $\chi \leq 1$, we typically observe the single HDW-lines to start directly at the IEX (Figure S4a). As the charge ratio increases, we observe the evolution of sharply bordered, more or less drop-shaped exclusion zones of increasing size (see also Movie S6).

Bright field images and tracer flow fields corresponding to the dark field images in Figures S4a, b, and d are presented in Figure S5. In Figure S5a, we studied the low-charge tracers on a native substrate. Here, the tracer motion directly reflects the underlying DO-flow field. In Figures S5b and c, we used larger charge ratios, but left all other boundary conditions unchanged (tracer concentration, exchange rate, IEX velocity). Therefore, the underlying solvent flow pattern must remain unaltered. In Figures S5b and c, however, we now see a significant alteration of the tracer flow field.

With increasing charge ratio, DP flows gain in strength and importance. Hence, tracers approaching the IEX at its front are stalled already at some distance to the IEX, while tracers initially located in the immediate vicinity of the IEX move outward (Figure S5c). A tracer depleted region forms. Comparison to the bright field images shows that tracers accumulate exactly where outward DP motion and inward DO flow balance and the tracer velocity vanishes: $v_T = v_{DPT} + v_{DO} = 0$. As the IEX passes, the accumulation region first shifts outward, then inward again. Tracers in this boundary are carried along as it shifts inward again (Figure S5b). The evolution of the drop-shaped formation zone in Figures S4a-d is thus seen to originate from changes in the location, where outward DP tracer motion and inward DO solvent flow balance.

Our observations can be rationalized considering that both DP and DO flows originate from the same electrophoretic effect (i.e., from the drop in chemical potential across a charged surface as induced by the increase in the pH of the adjacent solvent) but differ in the relevant type of surface and hydrodynamic boundary conditions. The DP flow originates on the tracer surface, i.e., it reacts to the tracer ζ-potential and the *local* pH gradient. Here, the theoretical concepts of bulk diffusio-phoresis in a quiescent solvent can be directly applied after suitable coordinate transformation.[1,2] By contrast, the DO flow in any volume element above the substrate originates from both the local contribution (depending on the substrate ζ-potential and the local pH gradient) and the *global* hydrodynamic flow pattern. The latter depends on the difference in pH between IEX surface and the background solvent but is also subject to modifications by the hydrodynamic boundary conditions of an extended substrate (and of a closed cell of finite volume). Such a situation is not analytically accessible but may be addressed in numerical calculations.[4] Note that therefore, DP tracer motion follows the local

gradient direction and DO solvent motion need not be co-linear.[5] This can clearly be seen comparing the solvent flow field of Figure S5a to the tracer flow fields in Figures S5b and c.

The differences in the position dependence of the two flows become relevant at increased tracer ζ-potentials. Irrespective of ζ_T, the tracer DP velocity drops quickly with increasing distance to the IEX, respectively the distance from the trail ridge. As the local pH-gradient along and perpendicular to the trail ridge vanishes with increased distance to the IEX, it becomes negligibly small. By contrast, the DO flows – depending on the large-scale pH differences – are still active far past the IEX. They retain considerable strength, focus the line, and close the initial depletion zone (Figure S5b). A single line results. With increasing tracer ζ-potential, the closing point shifts further away from the IEX. However, the splits always close and a single line is obtained past the line focus as long as a single C-IEX45 is used. By contrast, using a pair of IEX approximately doubles the local pH-gradient while leaving the global pH difference between IEX surface and background unchanged. This shifts the minimum approach distance still further outward. Tracers are now accumulated along a contour far off the IEX center, where the inward DO flow is still very slow (Figure 1, main text). Thus, they can avoid inward transport by the DO flow after IEX passage. The DP split becomes stabilized (Figure S4e).

Quite frequently, an additional line is formed starting at the center of the IEX back (Figures S4f-h). Interestingly, it starts with some delay. Presumably assisted by fluctuations, few tracers reach the IEX, beneath which they are trapped by the solvent flows and expelled once the loading capacity of the IEX is reached. In this type of tracer accumulation at the IEX, the feeding rate is way smaller than by direct DO flow causing the delay. Simultaneously, the roller velocity slightly increases by some 5-10 % and the depleted region slightly stretches. Both indicates a phoretic contribution of the trapped tracers to the propulsion, as well known from modular swimmers.[6] Due to a low feeding rate, this line type typically contributes only little to the merged line in the decay regime.

1.4. Alternative ink, alternative pens

The modularity of our approach allows facile testing of the effects introduced by alternative components. By varying the size of silica tracers, both line graininess and contrast can be varied. This is demonstrated in Figure S6 for three species of Si tracers with different sizes as indicated. In all three cases, we used the same tracer concentration c = 0.1 wt.%. With decreasing tracer size, both graininess and contrast decrease. For the largest tracers, the lines obtain a “pointillistic” appearance. They become smoother at lower tracer size, but at the same time loose contrast, as scattering power scales with a_T^{-6}. Next, we exchanged the silica particles for Polystyrene particles of lower mass density (PS2.3, ρ_{PS} = 1.05 kg m^{-3}). Three representative images are shown in Figure S7.

The use of lighter tracers generally leads to lines blurred by convection. For tracers of low charge (Figures S7a and b), regions of enhanced density form way above the focusing DO flows along the substrate. For highly charged tracers (Figure S7c), the broadening is additionally enhanced by outward DP motion, which leads to an upward motion already at some distance from the IEX surface. Overall, the use of tracers with low mass density leads to very low contrast and thus, is not useful for writing.

We next checked different types of pens for their capacity to write lines. The examples in Figure S8 feature inert rafts of Si832 tracer particles. These were made by slowly drying Si832 suspensions. The rafts were either free to glide through Si832 or were fixed and passed

by the tracers. Short trails resulted, which mainly depended on the shape, orientation, and velocity of the rafts. Figure S8a shows a mobile raft simply ploughing through the tracer layer. Here, a region of enhanced tracer density forms at its front as well as a short tracer-depleted region in its wake. Figure S8b shows a triangular raft fixed in a hydrodynamically favorable orientation. As the tracers drift by, a short trail of slightly increased tracer density forms downstream. Lacking pH gradients, pens made of chemically passive rafts do not trigger DO flows. Line shape and contrast are therefore fully determined by the laminar flow field around these differently shaped and oriented objects. However, in all cases, only very short lines resulted, even at larger gliding velocities. Thus, without attraction, no useful lines are written.

We further replaced the cationic IEX by anionic IEX (A-IEX) and compile the main results in Figure S9. This resin type exchanges residual carbonate ions for OH^-. Thus, it increases the pH. A-IEX-L features large exchange rates for CO_3H^- available at concentrations of several $\mu molL^{-1}$. They create a pronounced pH variation of complex shape featuring a pH maximum at some distance to the IEX surface (Figure S9a).[5] On its outer side, i.e., pointing away from the IEX, the pH-field is contoured by an inverted gradient (blue arrow in Figure S9b). Small hydrogel-based A-IEX20 spheres show somewhat lower exchange rates and lower capacities. These create a simpler pH field with only negative gradients but of much weaker amplitude and are well suited as pens. Negatively charged tracers approaching from the front are pushed away (both in rolling direction and sideways) by the corresponding *outward* DO flow (Figure S9c). A tracer-depleted region past the A-IEX results. For combination with Si832, we found small AIEX-L splinters to be most suitable. This combination leads to a high-contrast inverted line (Figure S9d). Like the positive lines discussed above, also this line of negative optical contrast appears to be very stable in time (Figure S9e).

1.5. Alternative drive

In Figure S10, we again used tracers which are gravitationally bound to the substrate and cationic IEX. We here studied modular micro-swimmers, which propel on a horizontal substrate driven by the DP flow along the surfaces of assembled tracers (see also Movie S7).[6] In all three cases, we observe a characteristic shape of the formation zone, featuring a blob-like region of enhanced tracer density in the immediate back of the IEX. From that blob, a much finer line of tracers is expelled, which only slowly broadens by diffusion. Figure S10a shows a line written by tracers with different sizes past a cationic IEX resin splinter obtained from crushing a larger IEX bead.[7] It demonstrates that a spherical IEX geometry is not essential for writing, nor is a uniform tracer size. Figure S10b shows that, due to mutual repulsion between the negatively charged tracers, the raft past the IEX may take a crystalline structure. However, this has little influence on line formation. In Figure S10c, a modular swimmer is formed by exactly the same components as used in the writing experiments of the main text. Again, a nice line is written past a short formation zone of enhanced tracer density.

Figure S10 demonstrates that writing does not depend on the type of steering chosen. Rather, it requires the presence of an effective attraction (here realized by DO flows). However, modular swimmers lack the ability of precise steering, they steer by statistical rearrangements of their load. Therefore, these freely propelling modular swimmers write curves instead of straight lines or prescribed patterns. In the approach presented in the main text, propulsion by

gravity was essential for writing straight lines as prerequisite for drawing more complex patterns.

2. Additional Data from Theory

2.1 Extracting an effective potential

To model the non-reciprocal effective force between the IEX and the tracer particles, we fitted the tracer velocity field behind the IEX by using different functional forms (Figure S11). The fit was done on the logarithmic scale using the nonlinear least-squares method. The goodness of each fit is measured by the normalized mean-squared distance of the fit values f_i to the data values d_i on the logarithmic scale:

$$\chi^2 = \sum_i \frac{[\ln(d_i) - \ln(f_i)]^2}{\ln(d_i)}. \quad \text{(S1)}$$

We found that the functional form given in Equation (1) in the main text provides a good fit to the data. Unlike the other shown fits (dashed-dotted and dotted lines) it also captures the plateau for $r \to 0$ and leads to a reasonable extrapolation capturing the expected power-law decay for $r \to \infty$ (Figure S11).

2.2. Reaching the stationary state

In the numerical calculations, the IEX is fixed at $x = 0$ in a homogeneous background of tracer particles at $t = 0$ moving at constant speed v_{IEX}. In Figure S12, we show the temporal evolution of the line amplitude in terms of the central probability density $p(t, x, 0)$ on the path of the IEX at certain distances behind the IEX. In Figures S12a-c, we fixed the diffusion coefficient $D = 0.5\ \mu m^2 s^{-1}$ and varied the IEX speed v_{IEX}. We obtain two types of curves reaching a stationary state within the investigated time span of 2000 s. At large v_{IEX}, a stationary state for p is reached within 100-400 s with a trivial dependence on x. The line amplitude plateaus well above the homogenous background. This corresponds to the single-line formation regime of Figure 4 in the main text. At small v_{IEX}, a stationary state for p is reached later after some 500-700 s. Notably, the line amplitude reaches a plateau below the homogeneous background. This corresponds to the inverted line formation regime of Figure 4 in the main text. Interestingly, in both types of stationary state, the plateau amplitude decreases with increasing v_{IEX}. We attribute this to the smaller number of attracted and/or trapped tracer particles (Figure S2). For speeds v_{IEX} in the transition region between inverted and single lines, the time to reach a stationary state significantly increases because the IEX traps a large amount of tracer particles, which can later escape the trapping region if the number of trapped tracers is large enough. In Figures S12d-f, we fixed the IEX speed to $v_{IEX} = 8.6\ \mu m s^{-1}$ and varied the diffusion coefficient. The chosen x are located past the line focus. The plateau amplitude decreases for increasing D.

To further study the line amplitude relaxation, we fitted the Gompertz equation

$$p(t) = p_0 \exp\left(-\exp\left[-\frac{t-\Delta t}{\tau}\right]\right) + p_{\text{offset}} \quad \text{(S2)}$$

with stationary central amplitude p_0, time delay Δt, amplitude relaxation time τ, and background amplitude p_{offset}.[8] The fit results are shown in Figure S13. The amplitude relaxation time linearly decreases with the distance x to the IEX (Figure S13a). For a typical distance of 500µm past the IEX, corresponding approximately to the dimension of a single

letter, the stationary state is reached with an amplitude relaxation time of $\tau \approx 30$s. Furthermore, the stationary central amplitude shows a power-law dependence on the distance x (Figure S13b) caused by diffusion processes. The time delay Δt of the amplitude relaxation increases linearly with x with a slope equal to the IEX speed (Figure S13c). The time to reach the stationary state hardly changes with varying D and only shows a weak logarithmic dependence (Figure S13d). However, it decreases with increasing IEX speed (Figure S13f). The stationary central amplitude decreases with both the diffusion coefficient and the IEX speed (Figures S13e and g).

2.3. Line formation zone

In the line formation zone at very small distances, a split line is observed in the model that merges to a single Gaussian-shaped line at intermediate distances (Figures S14a-c). Past the merging distance, the line first narrows further but eventually broadens as the tracer attraction vanishes and diffusion begins to dominate the tracer motion. The location of this line focus, which separates the line formation zone from the decay zone, defines the line formation length. The latter can be accurately determined via the x-dependent standard deviation of Gaussians fitted to the line profiles observed at different IEX speeds (Figure S14). The distance at which the line shows a minimum standard deviation is identified as the line formation length (dashed lines in Figure S14d). The line formation length increases with increasing v_{IEX}. For $v_{IEX} = 8.6$ µm s^{-1}, we find $l_f = 90$ µm in good agreement with the experimental observations.

2.4. Discrimination of line types

In the stationary state at $t = 2000$ s, we fitted single Gaussians and the sum of two equal Gaussians to the line profiles determined at $x = -950$ µm, i.e., way past the line focus. Figure S15 shows three examples for the three typical line shapes: inverted line, single line, and split line (see also Figure 4, main text).

2.5. Trail formation at early times

Since our minimal model is solely based on the long-range tracer transport towards the IEX and restricted to two dimensions, it is of course not capable to reproduce the detailed tracer motion close to the IEX within the formation zone. In Figure S16, we show the trail formation in the BD simulation with point-like tracer particles at early times. Due to the constriction of the tracer motion to two spatial dimensions, a small layer of tracer particles accumulates at the front and sides of the IEX ($2a \approx 23$ µm, c.f. inset of Figure 3a, main text). Interestingly however, the trail formation behind the IEX is qualitatively similar to the experimental observations. Accumulation at the front is not seen in the experiments because tracer particles can either be swept further underneath the IEX sphere or escape this region by moving along the third spatial dimension due to strong upward solvent flows in the vicinity of the IEX.

2.6. Density dependence of the line shape

Thus far, we neglected interactions (volume exclusion) between the tracer particles. Considering repulsive tracer-tracer interaction $u(r)$ modelled by the Weeks-Chandler-Anderson potential[9] with strength $\varepsilon = 10 k_B T_{bath}$ and effective particle diameter $\sigma = 2a_T$ grants interesting insights into the limits and capabilities of our minimal model:

We studied the line shape for interacting tracer particles at different tracer area fractions $\varphi \in \{0.030, 0.076, 0.152, 0.304\}$ which correspond to tracer concentrations of 0.02 wt.%, 0.05

wt.%, 0.10 wt.%, and 0.20 wt.%, respectively. Figure S17 shows simulation snapshots after t = 110 s for the different tracer concentrations as well as the density profiles at x = 500µm. For higher concentrations, the line width increases. Remarkably, and in contrast to the experimental results (Figure 2d, main text), the line shows a Gaussian shape only at small tracer concentrations. At high concentrations, the shape features a broader, non-Gaussian peak caused by the restriction of the tracer motion to the 2D plane. This contrasts with the model calculations using point-like tracers, which can accumulate to arbitrarily large densities, and to the experiments, where particles may escape to higher elevations. We anticipate that flattening should become observable in experiments using tracers of large density mismatch, which stay settled and cannot escape to the third dimension.

The effects of tracer-tracer interactions have interesting implications on the difference between our experimental and theoretical results: First, the use of point-like tracers in the numerical calculations strengthens the trapping effect because more tracers can be trapped in the vicinity of the IEX as compared to the experiments, in which the tracers have a finite size. Trapping is readily visualized in the present experiments particularly at low IEX velocities (example IV in Figure 4c, main text). However, there, the trapped particles are either sheared off the assembly at its sides, creating a short, diffusively dispersing double line feature, or they are expelled at the back of the assembly, thus filling any underlying depletion zone. As a result, no well-defined density variation (line) emerges, neither under- nor over-density. At larger velocities of $v_{IEX} \approx$ 8-10 µm s^{-1}, and in particular, for native substrates of large ζ-potential, the DO flow may be sufficiently strong to create a noticeable underdensity (Figure S4a). However, only a small number of attracted tracers becomes trapped at large velocities. Rather, they are immediately expelled to the back. Thus, we observe a shallow depletion zone to both sides of a strong HDW-line, which extends way beyond the HDW-line focus. The shallow underdensity serves to enhance the optical contrast.

3. Accuracy of writing patterns

In the simulations, we prescribe IEX trajectories within the simulation box. Written lines follow these quite accurately, as illustrated in Figure S18. Two small, unavoidable deviations are, however, obvious: First, tracers assembled in the line past the IEX are drawn towards the IEX at its actual position. This originates from the long-ranged nature of the attraction. It leads to an inward offset in the written spiral as compared to the prescribed trajectory (Figure S18a), a right shift in the line crossing event shown in Figure S18b, and a "short-cutting" of turns with small radius of curvature (Figure S18c). In principle, all these effects can be compensated for by appropriate anticipation and fine tuning of the prescribed trajectory (see the writing of the T in TUDa in Movie S5 for instance). The second effect is a local increase in line strength and density upon line crossing events (Figures S18b and c). This local effect occurs, as the IEX acts on the already enhanced density in the immediate environment. Depending on the IEX speed, the corresponding short over-dense region (blob) is shifted in the direction of the effective attraction. The blob occurs past the crossing point. This effect cannot be cured but gets less pronounced for larger velocities.

The line shifts due to attraction are even more pronounced in experiments and increase with increasing substrate charge leading to more pronounced DO flows towards the IEX (c.f. the solvent flow trajectories shown in Figure S5). Blob formation is also present but can be minimized for writing with high IEX velocities $v_{IEX} \geq 10 \mu m s^{-1}$. Yet another effect becomes prominent in experiments attempting to draw complex figures. This is highlighted by yellow encircling in Figure S19. If the pen moves on an already drawn line, its velocity is altered. If it moves against the former propagation direction, it is slowed. This shortens the written line as

compared to the programmed trajectory. Moving in the opposite direction, its velocity is increased, and the written line becomes more extended than programmed. Lines are also lengthened if they approach an already written line from an angle. Likewise, lines written such as to pass in the immediate vicinity of an already finished line part get shifted towards the latter. Together, this tends to wreck figures with many line crossings. However, such effects can be accommodated by variation of the programmed stage tilting sequence. Going from Figures S19a-d, we successively adapted the programmed trajectory to make the drawn figure approach the desired one (inset in Figure S19d). While somewhat tedious, this step-by-step procedure is nevertheless successful. In future, it will be improved by replacing the manual programming by some learning package based on image processing feedback.

4. Blotted lines

Blob formation upon line-crossing has been discussed in the main text. Occasionally, we observe an additional type of blob formation. It is caused by a transient sticking of the IEX to the substrate. This process of blob formation is followed in a series of images in Figure S20. The blob is mainly formed by the trail catching up with the now-stuck IEX and further tracer accretion at the fixed IEX. Note that during sticking, the tracers slowly overtake the IEX. After detachment, the IEX velocity initially is slower than the final velocity. This is attributed to IEX friction with the locally enhanced tracer density but may further be related to altered DO flows. By contrast to blobbing upon line crossing, this type is not systematic. It therefore may be an issue already in straight line writing. Blobbing by transient sticking is most prominent for low-charge substrates and elevated tracer concentrations. It is also more frequent at lower velocities. Blob formation events are uncorrelated, and the resulting line appears to be blotted (Figure S20d). A regular blobbing pattern might be introduced for decorative purposes by transiently trapping the IEX by an optical tweezer for example.

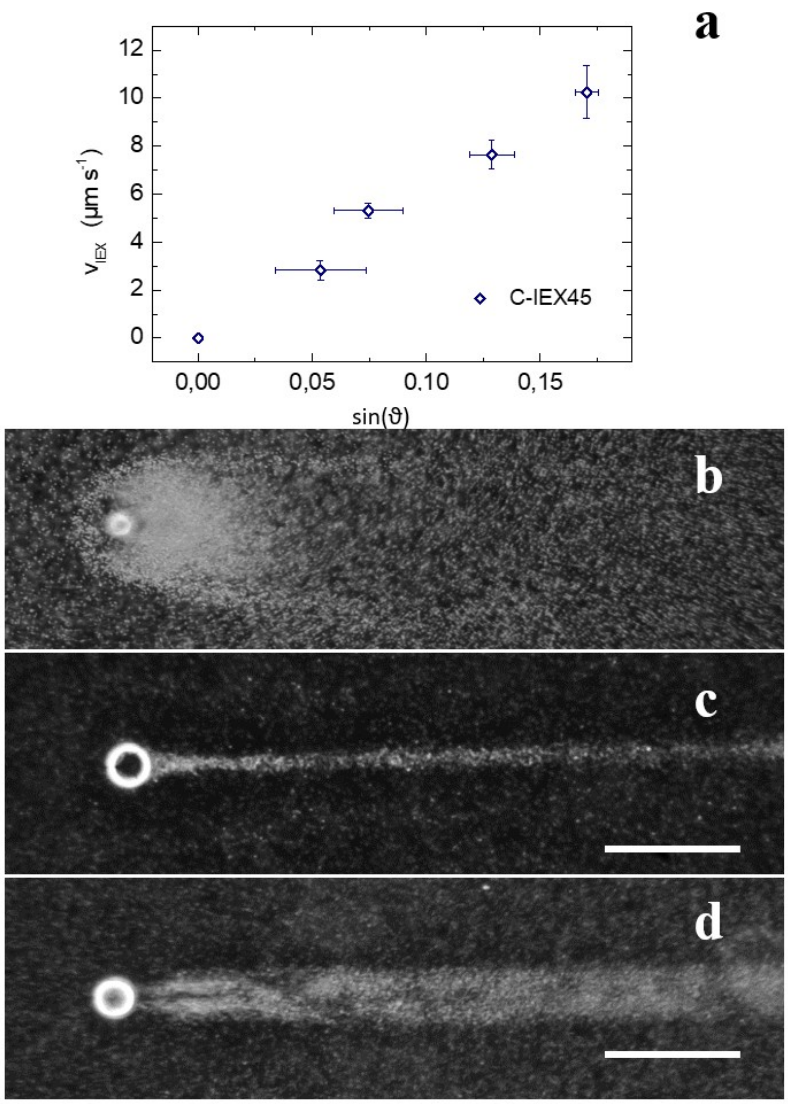

Figure S1. Tuning the inclination. a) Speed of C-IEX45 rolling through tracer free water as a function of substrate inclination. b-d) Dark filed images taken at different velocities of C-IEX45. Scale bars: 200 µm. b) C-IEX45 rolling through 0.1 wt.% Si2.1 at very low $v_{IEX} \approx$ 0.28 µm s^{-1}. Note the extended asymmetric accretion zone. No useful line is written. c) C-IEX45 rolling through 0.1 wt.% Si832 at v_{IEX} = 7.2 µm s^{-1}. A straight, narrow line is obtained. d) C-IEX45 rolling through 0.16 wt.% Si832 at v_{IEX} = 14 µm s^{-1}. Note the initial line split, which quickly washes out due to diffusion.

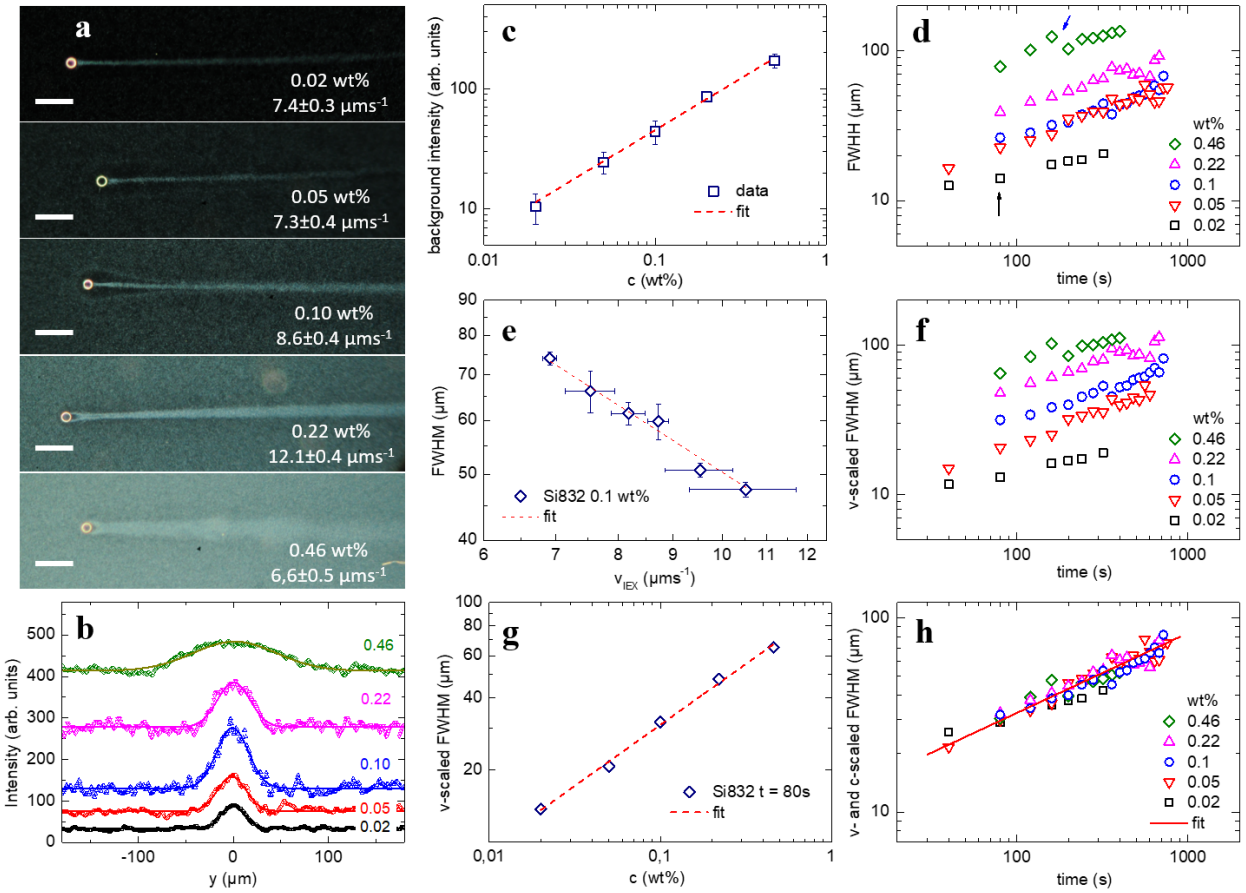

Figure S2. Line width measurements. a) Dark field snapshots of C-IEX45 rolling with speeds in the range of 6-12 µm through Si832 of different concentrations as indicated. Scale bars: 200 µm. Concentrations and speeds are indicated in each image. b) Line profiles recorded 80 s after IEX passage. The solid lines are fits of a Gaussian with an offset corresponding to the background scattering intensity. c) Double-logarithmic plot of the concentration dependent scattered intensity in dark field images of tracers equilibrated on a horizontal substrate. The fit of a linear function to the data returned a power law exponent of $a = 0.85 \pm 0.04$. d) Double-logarithmic plot of the time dependent FWHM for the five experiments shown in panel (a). e) Double-logarithmic plot of the dependence of line width on IEX speed for C-IEX45 rolling through Si832 at 0.18 wt.%. The fit of a linear function to the data (dashed line) returns a power law exponent of -1.02 ± 0.09. f) Double-logarithmic plot of the time-dependent FWHM scaled to $v_{IEX} = 8$ µm s^{-1}. g) Double-logarithmic plot of the v-scaled FWHM in dependence on Si832 concentration. The fit of a linear function to the data (dashed line) returns a power law exponent of $a = 0.51 \pm 0.02$. h) Double-logarithmic plot of the time-dependent FWHM scaled to $v_{IEX} = 8$ µm s^{-1} and $c = 0.1$ wt.%. The fit of a linear function to the complete data (solid line) returns a power law exponent of $\lambda = 0.48 \pm 0.04$.

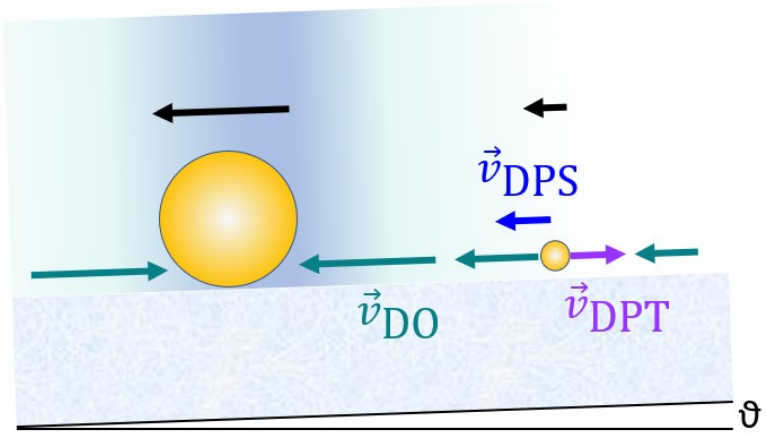

Figure S3. Relevant velocities during tracer approach. Due to gravity, both IEX and tracers roll at speeds v_i down the substrate tilted by ϑ (black arrows). The incompressible solvent flows with local velocities $v_{DO}(x,y)$ under the influence of the pH field (indicated by the background shading). The DO flow accelerates as it converges at the IEX (green arrows). The pH-gradient further induces a diffusio-phoretic (DP) slip at the charged tracer surfaces. This results in an inward solvent flow (DPS, dark blue arrow) relative to the tracer surface and an outward tracer motion (DPT, violet arrow).

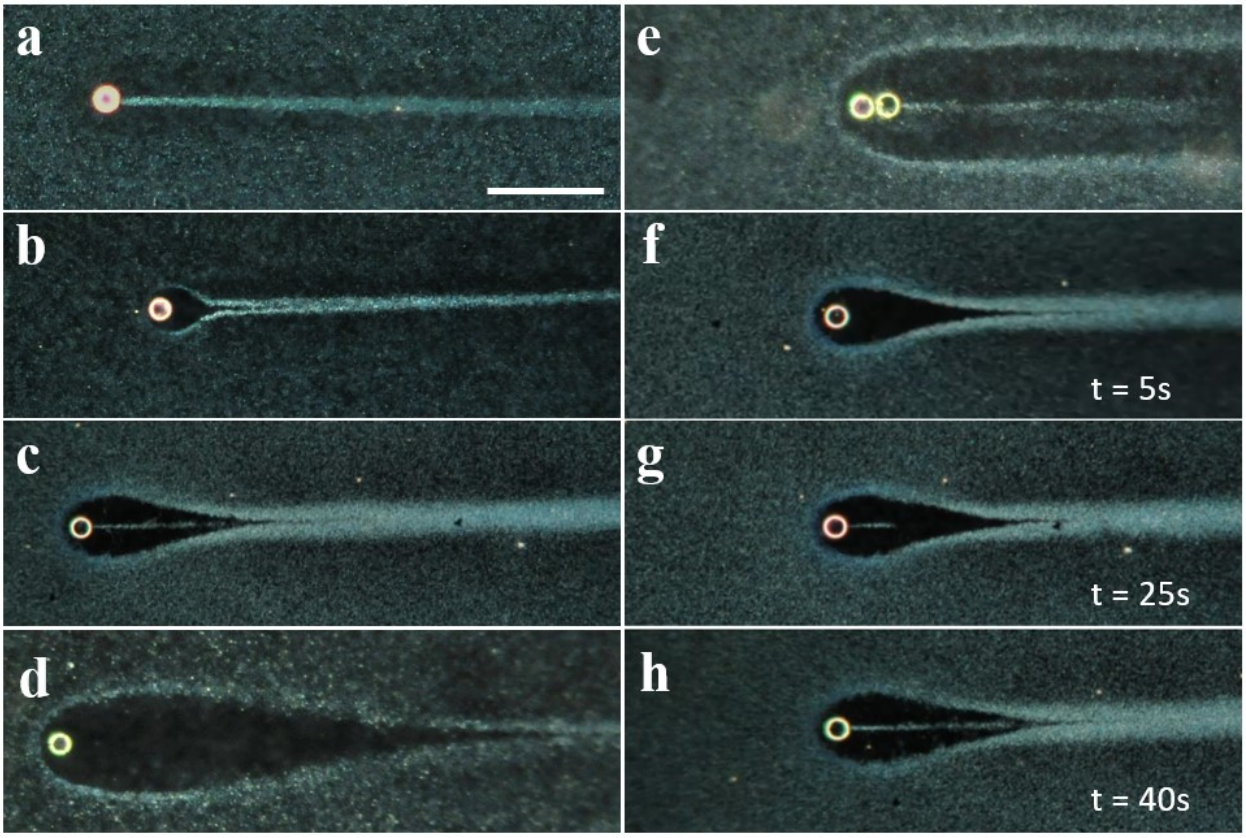

Figure S4. Manipulating the shape of the line formation zone. Dark field images of CIEX45 rolling through Si832 at $\vartheta = 3.1$ ($v_{IEX} = 7.7$ µm s^{-1}). Scale bars: 200 µm. We here changed the minimum approach distance by varying the charge ratio χ. a) 0.02 wt.% Si832, salt free but non-decarbonized ($\zeta_T = -68$ mV) on a native substrate of $\zeta_S = -105$ mV. Note the slight depletion of Si832 from the immediate IEX surroundings. b) Same as in a, but after de-carbonizing Si832 for 1h ($\zeta_T = -80$ mV) and on a deconexed substrate ($\zeta_S = -70$ mV). c) Same as in panel (a), but after de-carbonizing Si832 for 24h ($\zeta_T = -102$ mV) on a deconexed substrate ($\zeta_S = -70$ mV). d) Single IEX rolling in 0.16 wt.% Si832 deionized for 21d ($\zeta_T = -108$ mV) on a deconexed substrate ($\zeta_S = -70$ mV). e) IEX-pair rolling through 0.16 wt.% Si832 deionized for 21d ($\zeta_T = -108$ mV). f-h) Temporal development of the pattern seen in c. Snapshots were taken at different times after the start of the experiment as indicated in the key.

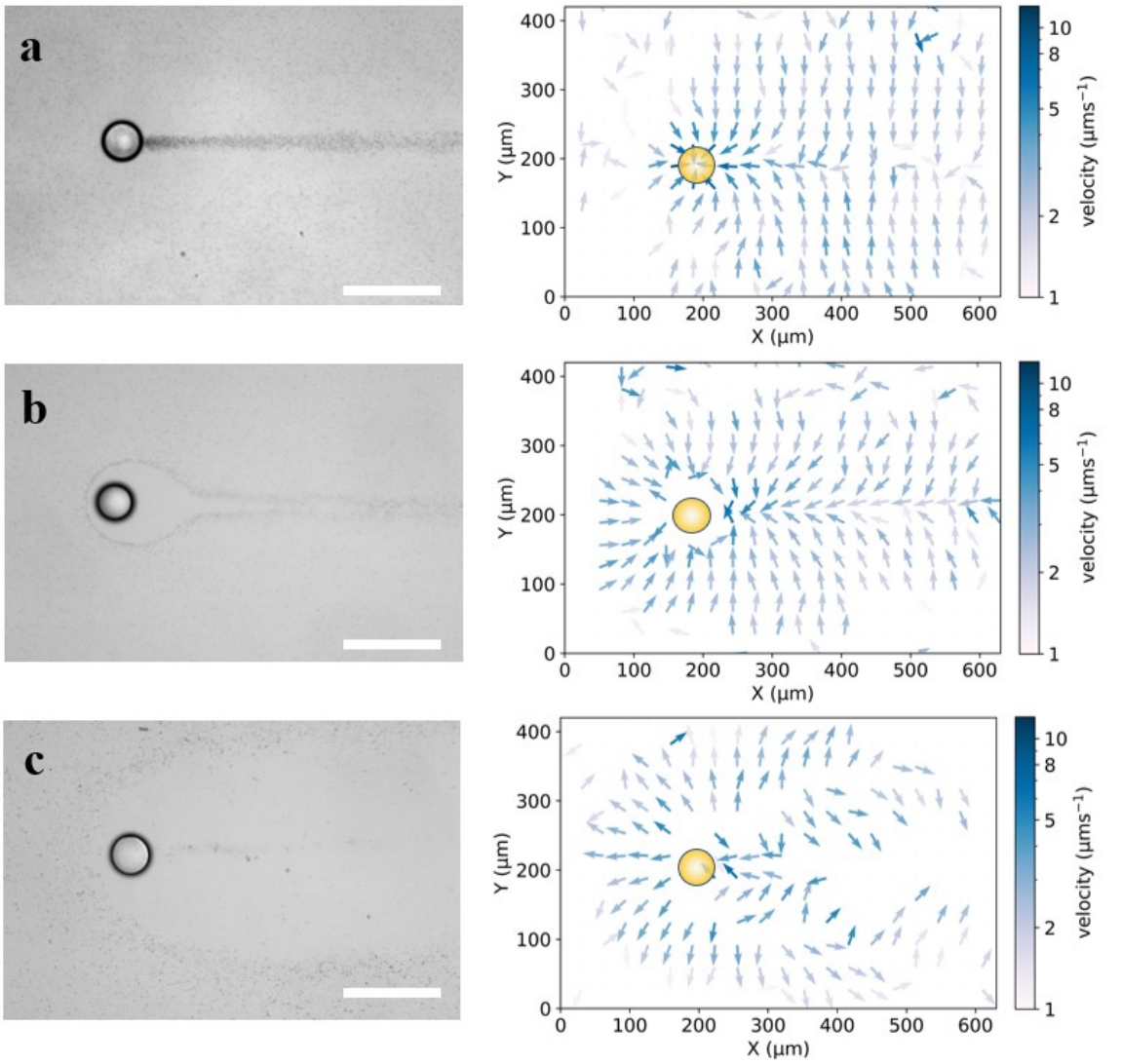

Figure S5. Flow analysis. Bright field images (left, scale bar 100 µm) and tracer flow fields (right) for C-IEX45 rolling at 3.1° inclination (v_{IEX} = 7.7 µm s^{-1}). The flow direction is given by the orientation of the arrows and the instantaneous lab-frame velocity is encoded by the arrow color as indicated in the key. Images and maps were recorded for C-IEX45 rolling on differently charged glass substrates through 0.10 wt.% Si832 tracers. a) Salt free but not de-carbonized tracers (ζ_T = -68 mV) on a native substrate of ζ_S = -105 mV (same conditions as in Figure S4a). Under these conditions, DP flows are negligible and the tracer flow field coincides with the solvent flow field. b) Si832 deionized for 1h (ζ_T = -80 mV) on a deconexed substrate of ζ_S = -70 mV (same conditions as in Figure S4b). The tracer flow field shows significant differences when compared to the previous situation. c) Si832 deionized for 21d (ζ_S = -108 mV) on a deconexed substrate of ζ_S = -70 mV (same conditions as in Figure S4d). Note the now extended region of outward tracer motion next to the IEX in the velocity maps.

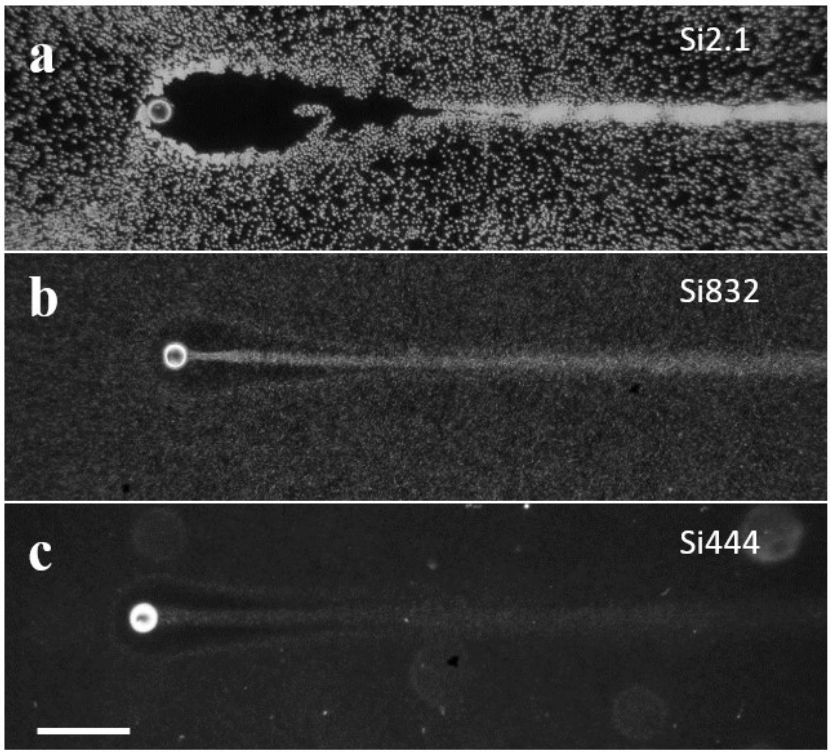

Figure S6. Variation of graininess and optical line contrast. Moderately de-carbonized C-IEX45 rolling at v_{IEX} = 8.4 µm s^{-1} on low-charge substrates. Scale bar: 250 µm. a) Si2.1 at c = 0.1 wt.%. b) Si832 at c = 0.1 wt.%. c) Si444 at c = 0.1 wt.%.

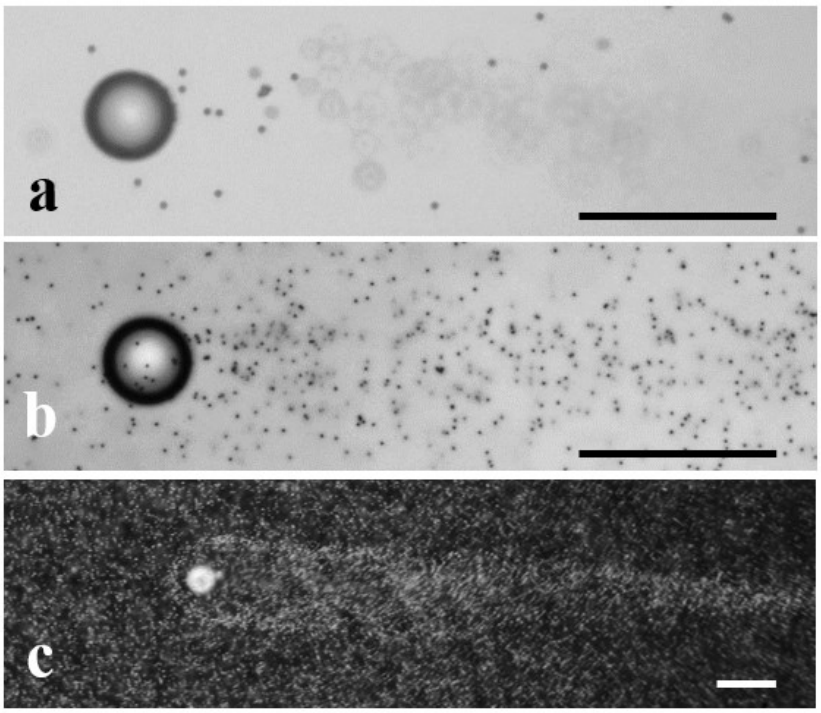

Figure S7. Weak-contrast lines written by C-IEX45 in different suspensions of light tracers. Scale bars: 100 µm. a) Bright field image of C-IEX45 rolling on an inclined substrate (ϑ = 2.3°) in a dilute suspension of PS2.3 (ζ_T = -35 mV). The tracers in focus approach the C-IEX along the substrate. The actual trail forms above (blurred tracer images). b) The same situation but now focused to some 150 µm above the substrate. c) Dark field images of C-IEX45 rolling on an inclined substrate (ϑ = 2.3°) in suspension of decarbonized PS2.3 (ζ_T = -65 mV) at 0.10 wt.%.

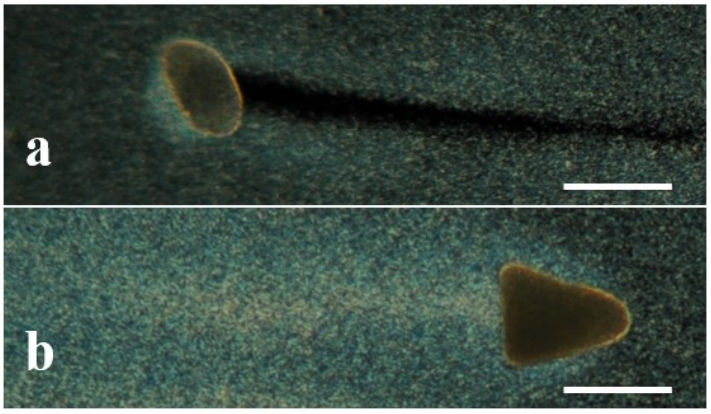

Figure S8. Writing with inert objects. Dark field images of weak trails formed by inert objects moving through suspensions of tracer particles. Scale bars: 100 µm. a) Chemically inert raft of dried Si832 gliding down an inclined substrate (ϑ = 7.6°) in a suspension of Si832 at 0.10 wt.%. b) Chemically inert raft of dried Si832 fixed to an inclined substrate (ϑ = 7.6°) in a suspension of Si832 at 0.10 wt.%.

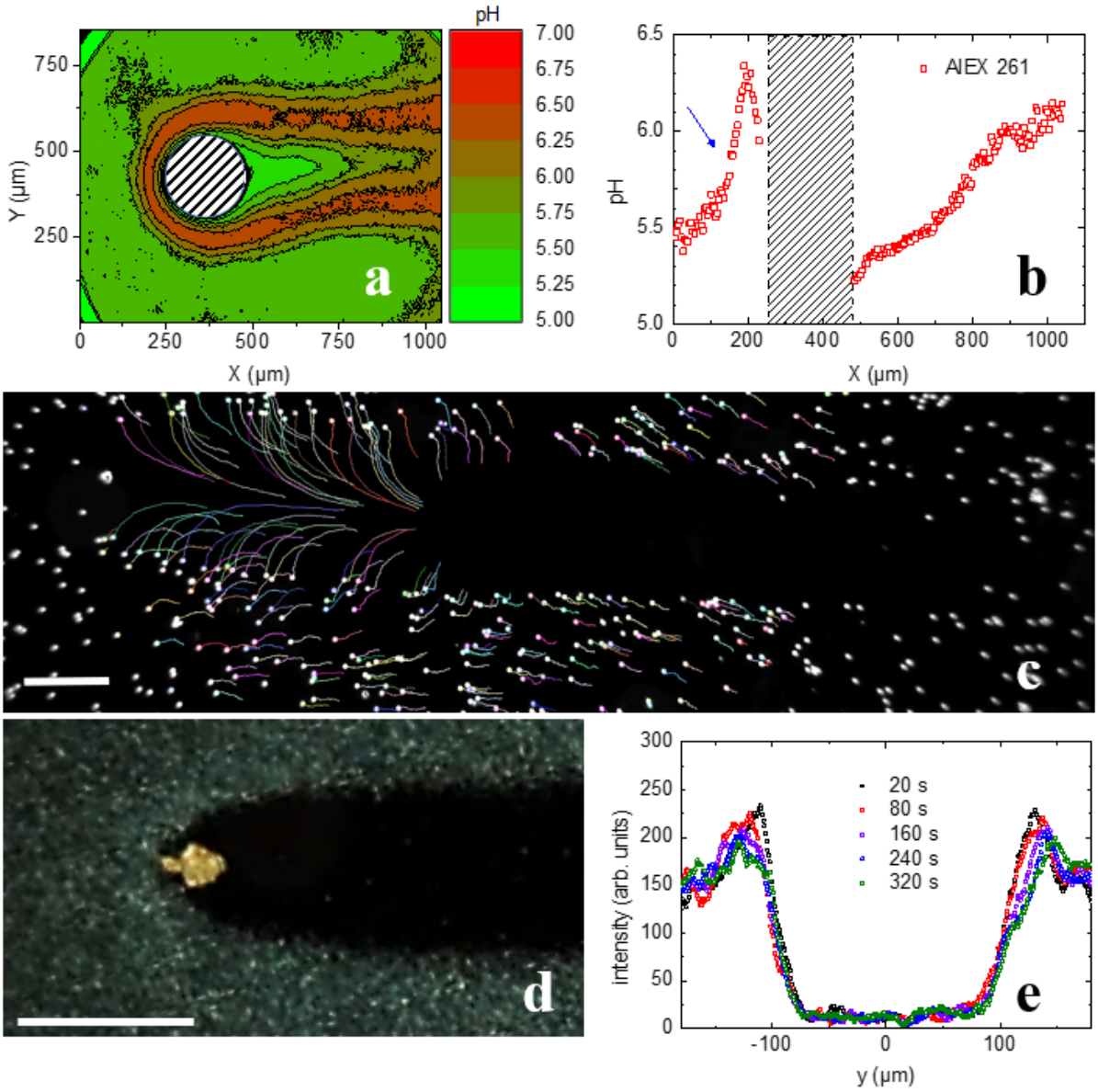

Figure S9. Contrast inversion by inversion of the pH gradient direction. a) pH-map of a resin-type anionic A-IEX-L of 261 µm diameter. Due to the high exchange rate, a complex pH pattern evolves. b) pH profile recorded along the rolling direction. The inverted gradient to the front of the AIEX is indicated by the blue arrow. Note however, that the whole pH-field is bordered by such an outward-decreasing pH field in panel (a). c) Tracer trajectories recorded in darkfield for a hydrogel-based A-IEX15. Scale bar: 200 µm. The ensuing pH filed is similar but less pronounced for this smaller resin species. Tracers are swept away from the A-IEX in forward direction and sideways. d) Small resin-type A-IEX-L splinter gliding down an inclined substrate in Si832 at 0.1 wt.% and creating a line of negative optical contrast. Scale bar: 250 µm. e) Line profiles of the inverted line drawn in (d) for different times after A-IEX passage as indicated.

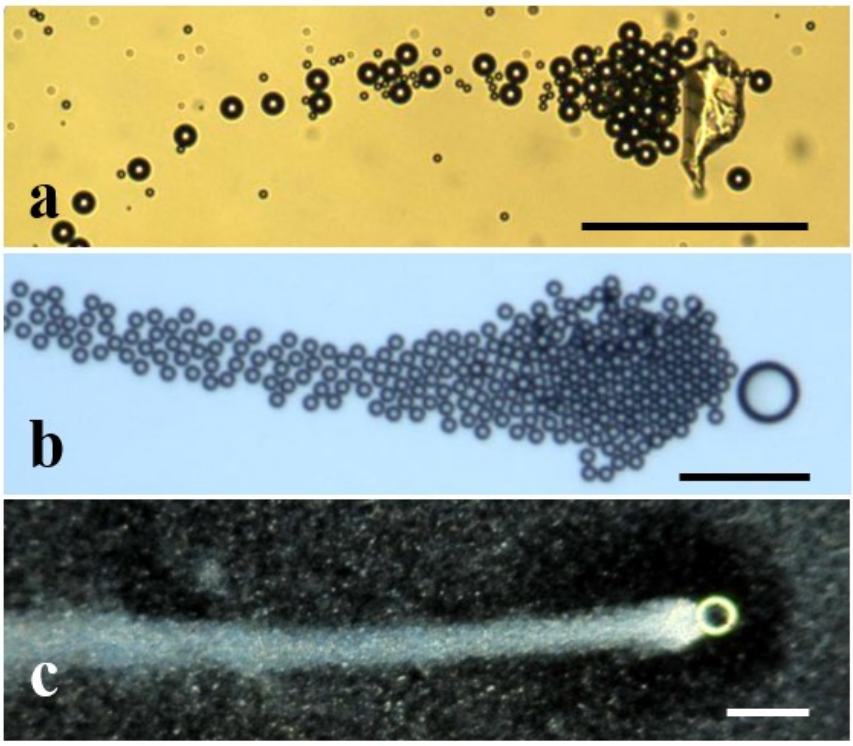

Figure S10. Writing with self-propelling pens. Images of lines formed by different cationic IEX types on horizontal native substrates in different tracer suspensions. These objects move as modular phoretic swimmers. Scale bars: 100 µm. a) Swimmer formed by a resin type C-IEX splinter in a dilute binary suspension of PS15, PS5.2 and PS1.7. b) Swimmer formed by microgel-type C-IEX45 in a dilute suspension of PS10. c) Swimmer formed by C-IEX45 in a suspension of Si832 at 0.10 wt.% on a horizontal substrate. Note the diffusely bordered depletion zone close to the C-IEX demonstrating the effect of the DO flows.

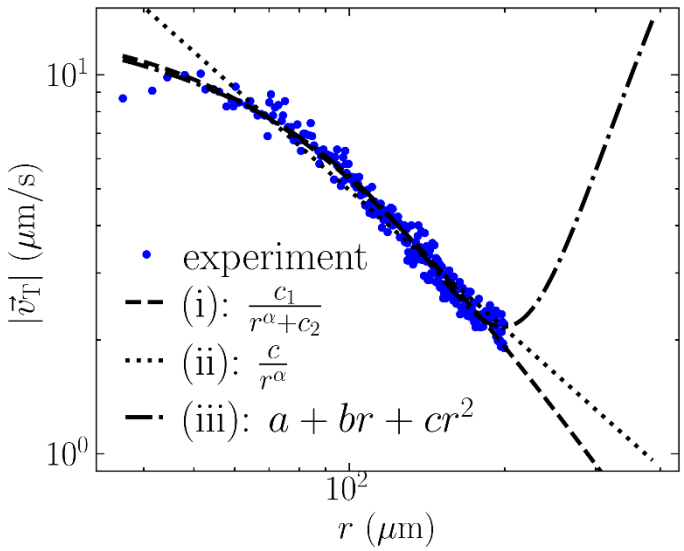

Figure S11. Nonlinear least-squares fits of the velocity field behind the IEX as used to extract a functional form of the effective interaction between IEX and tracers. The data is fitted on the logarithmic scale. The three shown fit functions (i)-(iii) have goodness 0.94, 1.55, and 0.81, respectively [see Equation (S1)]. Since fit (iii) results in an unphysical behavior at large distances and the simpler two-parameter fit (ii) has a significantly worse goodness, we finally used fit (i) which captures both the plateau at small *r* and the power-law decay at large *r*.

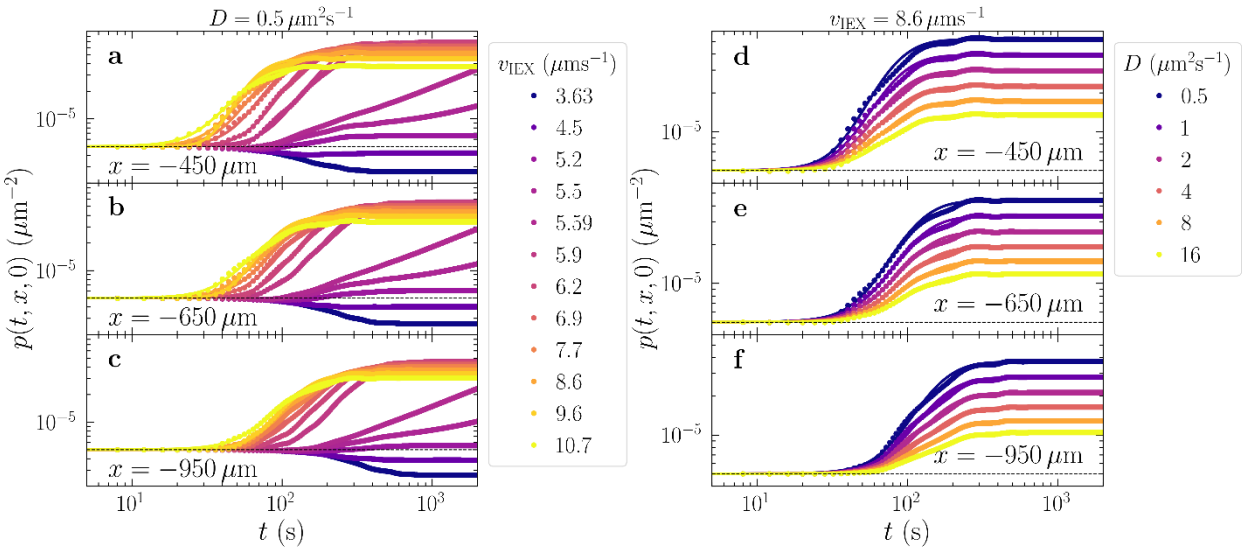

Figure S12. Time evolution of the line amplitude. Central probability density $p(t < 2000, x, 0)$ at different distances x from the IEX (values are given in the panels) as obtained from the numerical solution of Equation (6) in the main text. The solid lines are fits of Equation (S2) to the data. a-c) Data obtained for fixed diffusion constant $D = 0.5$ µm^2 s^{-1} and different IEX speeds v_{IEX} (color-coded according to the key). d-f) Data obtained for fixed IEX speed $v_{\mathrm{IEX}} = 8.6$ µm s^{-1} and different diffusion coefficients D (color-coded according to the key). Other parameters as given in Table 2 in the main text.

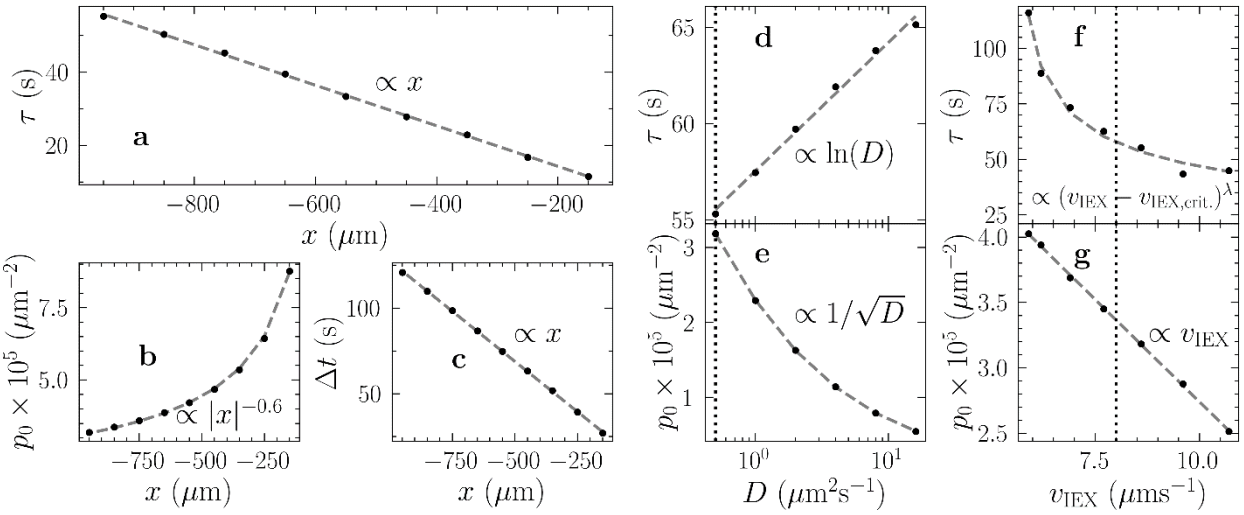

Figure S13. Analysis of the time evolution of the line amplitude as obtained from the fits shown in Figure S12. Black dots correspond to the respective fit parameters, grey dashed lines to fits as given in the key. a) Amplitude relaxation time τ, b) stationary central amplitude p_0, and c) time delay Δt over distance x to the IEX for D = 0.5 µm^2 s^{-1} and v_{IEX} = 8.6 µm s^{-1}. d) Amplitude relaxation time τ and e) stationary central amplitude p_0 as function of the diffusion coefficient for fixed v_{IEX} = 8.6 µm s^{-1} at x = -950 µm. f) Amplitude relaxation time τ and g) stationary central amplitude as function of the IEX speed for fixed D = 0.5 µm^2 s^{-1} at x = -950 µm. The critical IEX velocity $v_{\mathrm{IEX,crit.}}$ denotes the transition point from inverted to single lines. Vertical dotted lines denote typical values as used in the experiment.

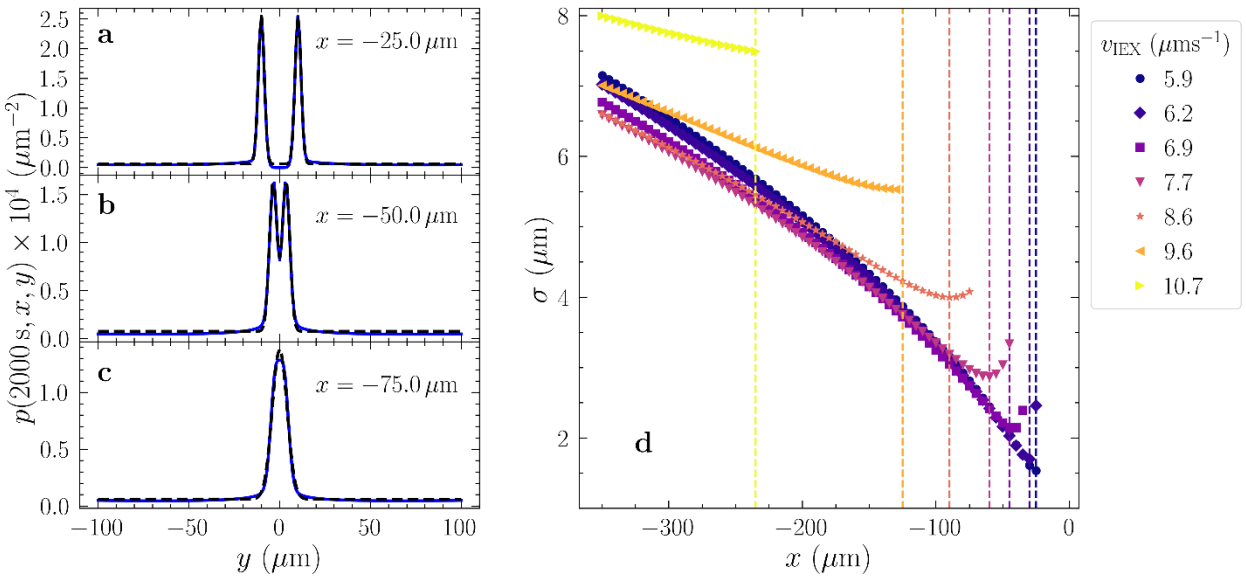

Figure S14. Determination of the line formation length. a-c) Line profiles for v_{IEX} = 8.6 µm s^{-1} and D = 0.5 µm^2 s^{-1} and d) line width for D = 0.5 µm^2 s^{-1} and different v_{IEX} obtained from the numerical solution of Equation (6) in the main text as a function of the distance past the IEX. The dashed black lines in panels (a)-(c) are fits to one Gaussian and a sum of two Gaussians, respectively. In panel (d), we show the standard deviation of the Gaussians fitted to the line profiles for different speeds v_{IEX} of the IEX (values are given in the key). A minimum coincides with the location of the line focus, whose position we denote as the line formation length (dashed vertical lines). For x closer to 0, the line is not a single Gaussian anymore but rather a split line. Therefore, the curves stop at certain x.

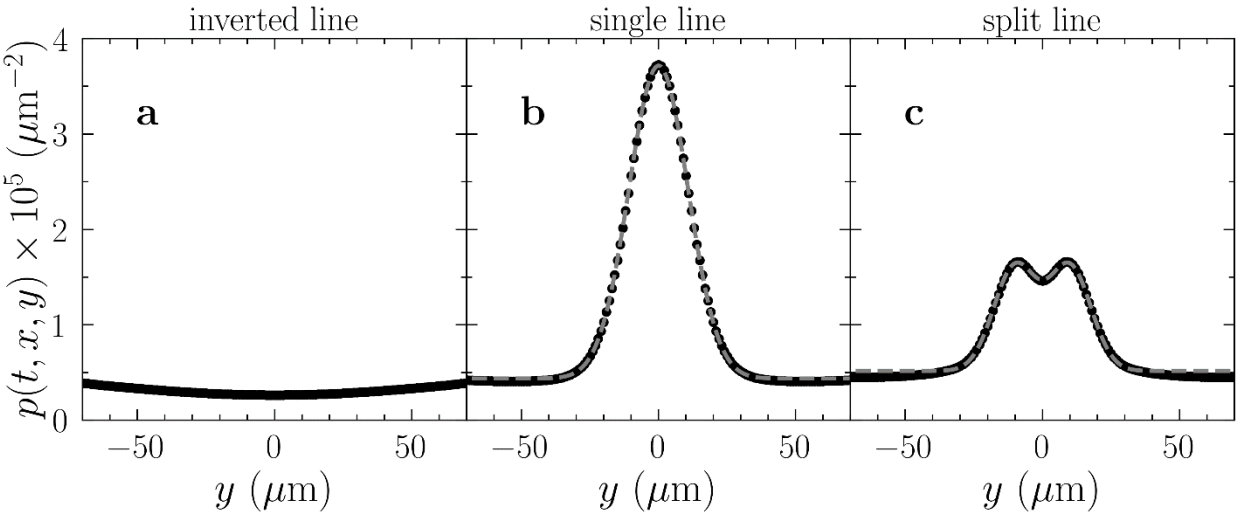

Figure S15. Analysis of line shapes. Exemplary line profiles obtained in the continuum model (Equation (6) in the main text) at t = 2000 s and x = -950 µm with D = 0.5 µm^2 s^{-1}. The dashed lines denote the corresponding fits of single or double Gaussians. a) v_{IEX} = 3.63 µm s^{-1}, b) v_{IEX} = 8.6 µm s^{-1}, and c) v_{IEX} = 16.4 µm s^{-1}. Note the pronounced differences in line amplitudes. All other parameters are given in Table 2 in the main text.

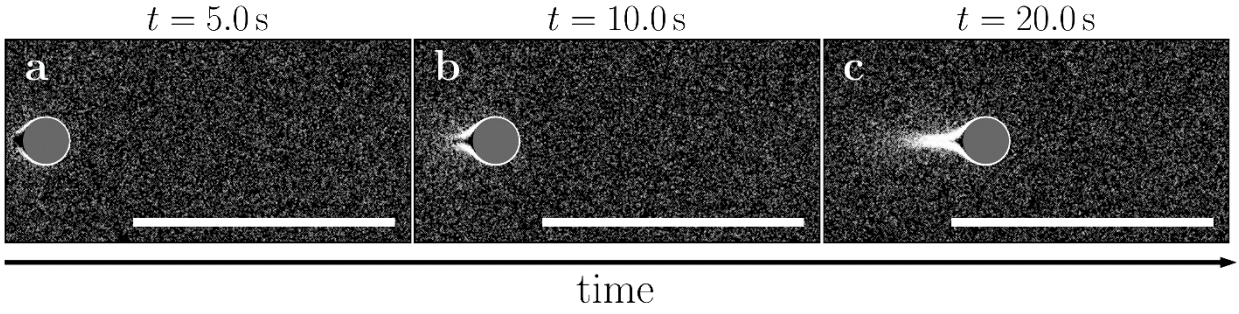

Figure S16. Short-time trail formation. Onset of writing for non-interacting tracer particles of radius a_T = 0.416 μm and diffusion coefficient D = 0.5 μm^2 s^{-1} at three different (early) times (a-c) ordered from left to right (values are given in the panels). The IEX moves at a speed v_{IEX} = 8.0 μm s^{-1} and the area fraction of tracer particles is φ = 0.152. All other parameters as given in Table 2 of the main text. Scale bar: 250 μm.

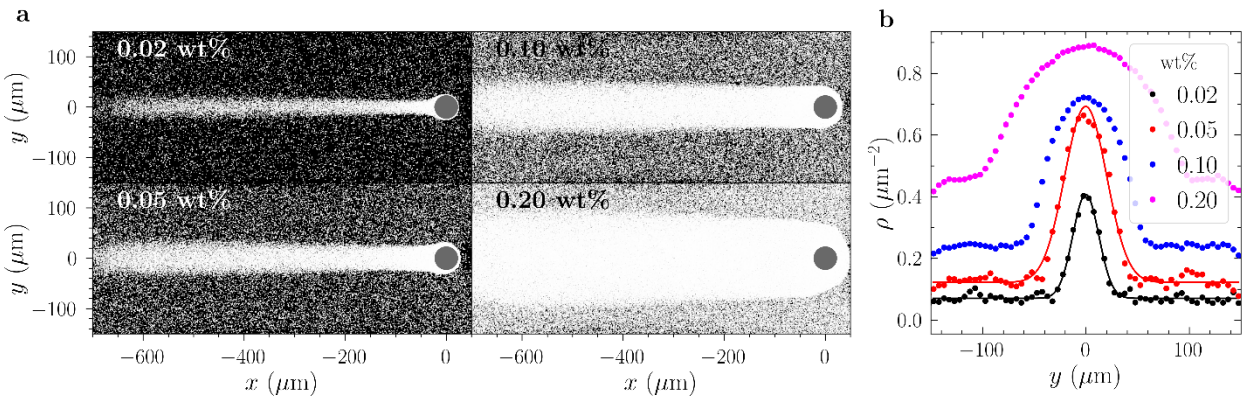

Figure S17. Density dependence of line profiles in Brownian dynamics simulations with repulsively interacting tracer particles of radius a_T = 0.416 µm and diffusion coefficient D = 0.5 µm^2 s^{-1}. The IEX moves at a speed v_{IEX} = 8.0 µm s^{-1}. a) Simulation snapshots after t = 110 s taken at different tracer concentrations (i.e., different area fractions) as indicated by the key. b) Corresponding line profiles obtained from averages over regions of 50 µm extension at a distance of x = -500 µm past the IEX. Solid lines are Gaussian fits, describing the data well at low tracer concentrations (i.e., area fractions). Other parameters are given in Table 2 in the main text.

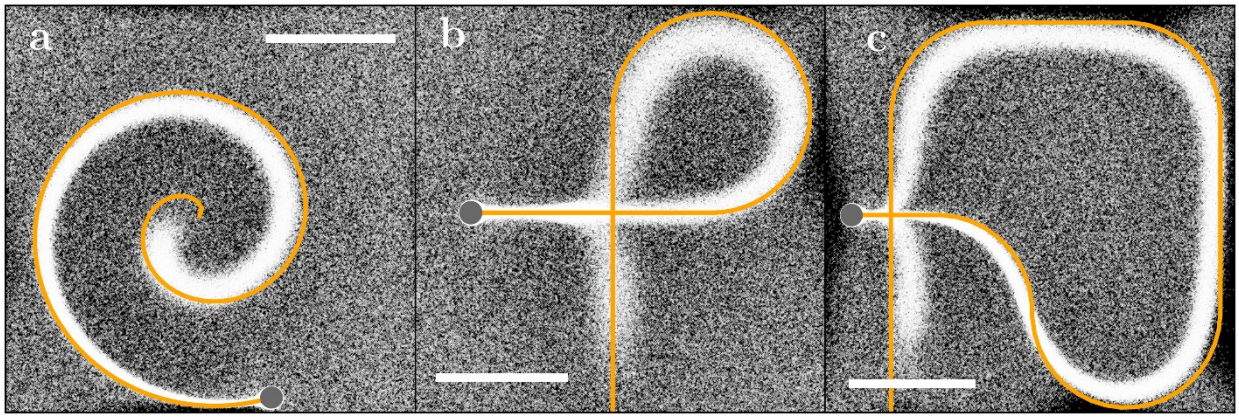

Figure S18. Exemplary patterns drawn in the BD simulation. Scale bar: 250 µm. a) Spiral. b) Clockwise loop with line crossing. c) The same as in panel (b) but crossing starting after an additional left turn. Note the blob just past the crossing and the slight deformation of the already drawn line. Simulation parameters are given in Table 2 in the main text.

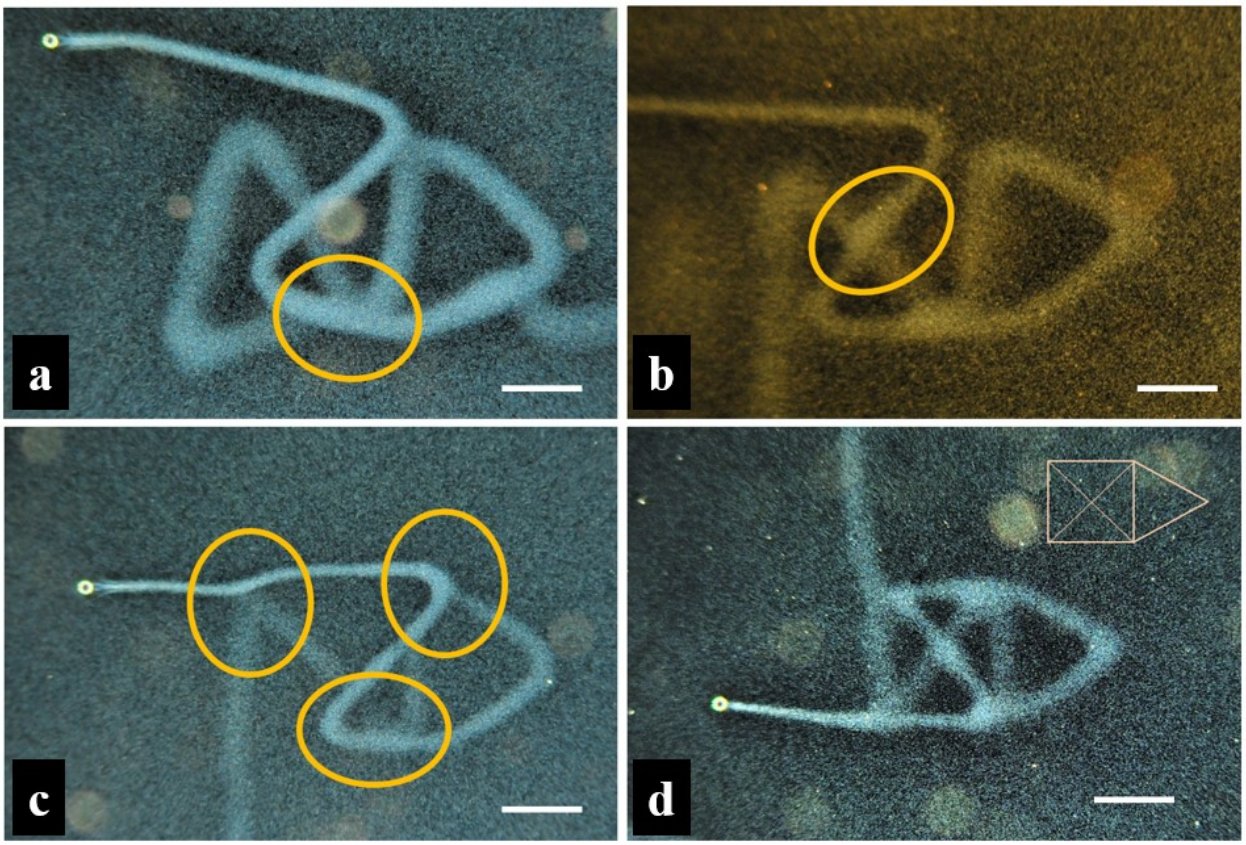

Figure S19. Approaching a perfect drawing in experiment. By trial and error, we successively improved the adjustment of the stage programming. Scale bar: 250 µm. a-c) Results obtained at intermediate stages. The encircled regions highlight deviations from the ideal pattern shape (line length variations, lateral line shifts, line bending, and blobbing, see Supporting Text). d) Final result.

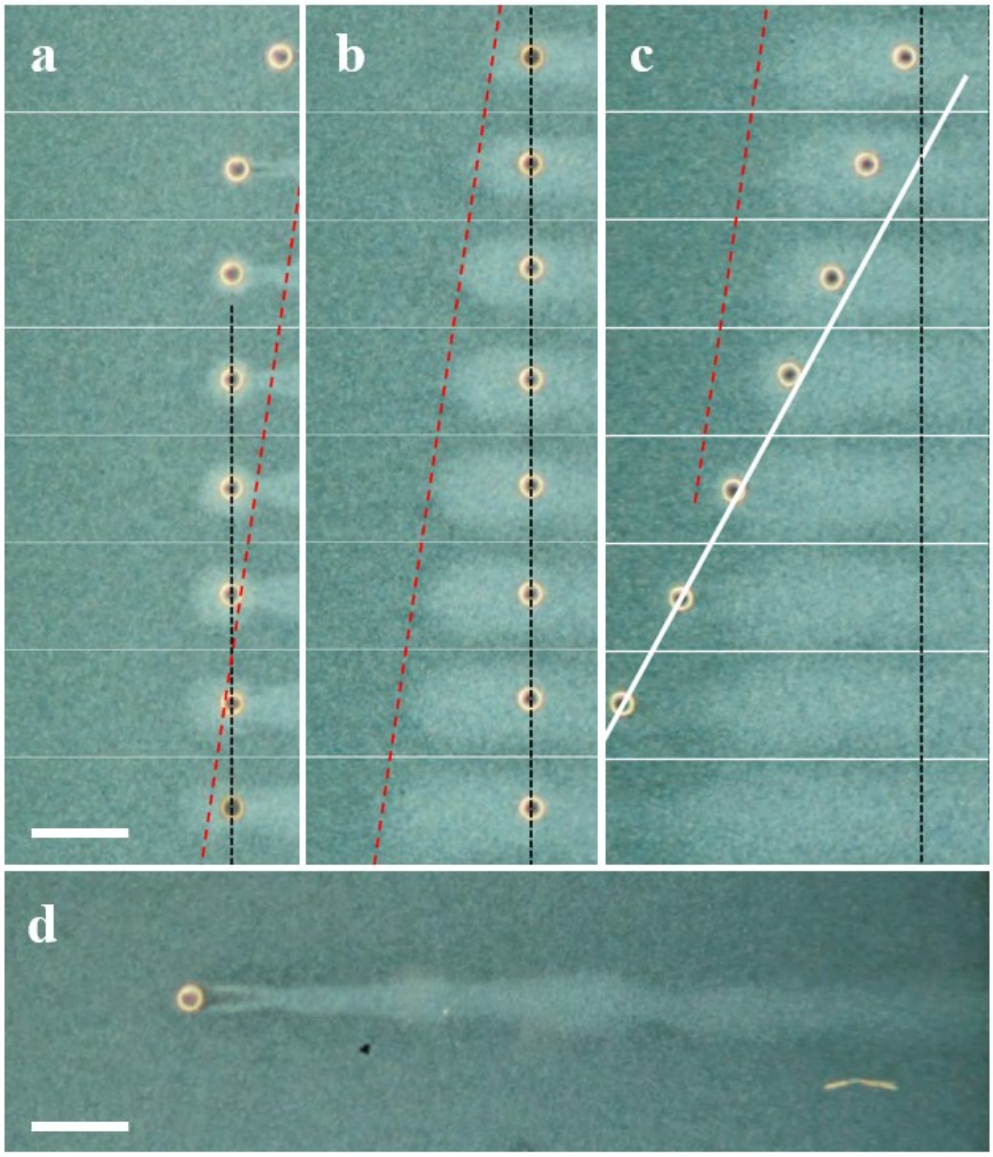

Figure S20. Formation of a blotted line. Time series of dark field images of blob formation due to a transient sticking of the IEX to the substrate. C-IEX45 rolling through Si832 at c = 0.2 wt.%. Scale bars: 250 µm. a-c) Development of a blob. Time increases from top to bottom and from panel (a) to (c). Images are separated by 800 ms. The dashed black line marks the position at which the IEX stuck to the substrate. The red line is a guide to the eye, marking the location of the blob tip, which continues to move leftward at roughly constant velocity, until the IEX is detached again. The solid white line denoted the constant velocity of the IEX after escaping the blob. Note the acceleration stage immediately after detachment. d) Frequent sticking results in blotted lines.

Movie S1.
CIEX45 in 0.1 wt.% native Si832 on a native substrate. Focus on line formation.

Movie S2.
CIEX45 in 0.1 wt.% native Si832 on a native substrate. Focus on line stability/decay.

Movie S3.
Brownian dynamics simulation of writing a straight line. Parameters as given in Tab. 2 in the main text.

Movie S4.
Numerical solution of the continuum model [Equation (6) in the main text]. Parameters as given in Tab. 2 in the main text but with $v_{IEX} = 8.6\,\mu m\,s^{-1}$.

Movie S5.
Writing "TUDa" in the Brownian dynamics simulation at $v_{IEX} = 12\,\mu m\,s^{-1}$. Other parameters as given in Tab. 2 in the main text.

Movie S6.
CIEX45 in 0.1 wt.% 2h deionized Si832 on a deconexed substrate. Focus on DP effects and changed flow field within the formation zone.

Movie S7.
Demonstration of modularity – writing with a self-propelling pen. CIEX45 in 0.1 wt.% native Si832 on a horizontal native substrate.

Movie S8.
Demonstration of erasing written letters by globally heating the system and recycling the ink in a Brownian dynamics simulation at $v_{IEX} = 12\,\mu m\,s^{-1}$. Other parameters as given in Tab. 2 in the main text. Scale bar: 250 µm.

Movie S9.
Demonstration of erasing a written line and rewriting at a shifted position by collecting the initial line with a second IEX following the "corrected" trajectory. CIEX45 in 0.1 wt.% Si832.

References

[1] J. L. Anderson, D. C. Prieve, *Sep. Purif. Methods* **1984**, *13*, 67.

[2] J. Anderson, *Annu. Rev. Fluid Mech.* **1989**, *21*, 61.

[3] P. Vogel, N. Möller, M. N. Qaisrani, P. Bista, S. A. L. Weber, H.-J. Butt, B. Liebchen, M. Sulpizi, T. Palberg, *J. Am. Chem. Soc.* **2022**, *144*, 21080.

[4] R. Niu, P. Kreissl, A. T. Brown, G. Rempfer, D. Botin, C. Holm, T. Palberg, J. de Graaf, *Soft Matter* **2017**, *13*, 1505.

[5] N. Möller, S. Seiffert, T. Palberg, R. Niu, *ChemNanoMat* **2021**, *7*, 1145.

[6] R. Niu, D. Botin, J. Weber, A. Reinmüller, T. Palberg, *Langmuir* **2017**, *33*, 3450.

[7] A. Reinmüller, H. J. Schöpe, T. Palberg, *Langmuir* **2013**, *29*, 1738.

[8] C. P. Winsor, *Proc. Natl. Acad. Sci.* **1932**, *18*, 1.

[9] J. D. Weeks, D. Chandler, H. C. Andersen, *J. Chem. Phys.* **1971**, *54*, 5237.